Theor. Comput. Fluid Dyn.
https://doi.org/10.1007/s00162-022-00623-0

ORIGINAL ARTICLE

Alessandro Ceci · Andrea Palumbo · Johan Larsson · Sergio Pirozzoli

Numerical tripping of high-speed turbulent boundary layers

Received: 25 March 2022 / Accepted: 18 July 2022

Abstract The influence of turbulence inflow generation on direct numerical simulations (DNS) of high-speed turbulent boundary layers at Mach numbers of 2 and 5.84 is investigated. Two main classes of inflow conditions are considered, based on the recycling/rescaling (RR) and the digital filtering (DF) approach, along with suitably modified versions. A series of DNS using very long streamwise domains is first carried out to provide reliable data for the subsequent investigation. A set of diagnostic parameters is then selected to verify achievement of an equilibrium state, and correlation laws for those quantities are obtained based on benchmark cases. Simulations using shorter domains, with extent comparable with that used in the current literature, are then carried out and compared with the benchmark data. Significant deviations from equilibrium conditions are found, to a different extent for the various flow properties, and depending on the inflow turbulence seeding. We find that the RR method yields superior performance in the evaluation of the inner-scaled wall pressure fluctuations and the turbulent shear stress. DF methods instead yield quicker adjustment and better accuracy in the prediction of wall friction and of the streamwise Reynolds stress in supersonic cases. Unrealistically high values of the wall pressure variance are obtained by the baseline DF method, while the proposed DF alternatives recover a closer agreement with respect to the benchmark. The hypersonic test case highlights that similar distribution of wall friction and heat transfer are obtained by both RR and DF baseline methods.

Keywords Direct numerical simulation · Boundary layers · Synthetic turbulence

1 Introduction

The prediction of supersonic turbulent wall-bounded flows is a subject of intense research within the fluid dynamics community. The establishment of solid scaling laws for friction and heat transfer rates in compressible boundary layers is crucial for the design of propulsive and thermal protection systems, especially in the case of strongly non-adiabatic conditions, which are typical of high-speed aircraft and aerospace hypersonic flight [36]. Whereas standard formulas and correlations developed for incompressible flows have shown to be quite successful when extended to supersonic flow under adiabatic conditions, the same does not apply to non-adiabatic walls. In this context, simple flow configurations as turbulent boundary layers over isothermal flat plates may be regarded as a good starting point for studying more complex flow configurations involving pressure gradients, impinging shock waves and conjugate heat transfer effects. Numerical simulations, based

Communicated by Julio Soria.

Alessandro Ceci (✉) · Andrea Palumbo · Sergio Pirozzoli
Dipartimento di Ingegneria Meccanica ed Aerospaziale, Sapienza Università di Roma, Via Eudossiana 18, 00184 Rome, Italy
E-mail: alessandro.ceci@uniroma1.it

Johan Larsson
Department of Mechanical Engineering, University of Maryland, College Park 20742, USA

Published online: 11 August 2022

on direct numerical simulation (DNS) and large-eddy simulation (LES) of the Navier–Stokes equations, are a suitable alternative to experiments for the study of such canonical flows.

Several numerical studies dealing with high-speed boundary layers have emerged in the last decades, probably starting with the work of Rai et al. [26] who first addressed the problem in a fully spatial setting. Pirozzoli and Bernardini [22,23] developed a DNS database for supersonic boundary layers under adiabatic conditions, which has been extensively used as a benchmark in later studies [43], which have also widened the Mach number range under scrutiny. Regarding hypersonic flow, pioneering DNS were carried out by Martín [18], with follow-up studies by Duan et al. [6,7]. DNS up to free-stream Mach number $M_0 = 20$ were carried out by Lagha et al. [15]. Zhang et al. [50,51] reported an extensive compilation of velocity, pressure and temperature statistics from $M_0 = 2.5$ to 14, for several wall cooling ratios, which is currently regarded as a reference in hypersonic flow studies.

A general issue encountered in all above-mentioned studies is the reliability and repeatability of the results. For instance, Poggie et al. [25] investigated effects related to grid resolution and domain width. A major source of discrepancy among different studies is associated with the imposition of the inflow conditions in spatially evolving simulations (e.g. Wu [47]). Sensitivity of boundary layer statistics to the upstream flow conditions is well known from studies dealing with incompressible flow [29,34], which also reflects experimental difficulties in achieving a fully developed state past tripping devices [8]. From a computational perspective, the most obvious way to overcome the problem has been using (more or less) long domains to allow attainment of an equilibrium state [33,34], and perhaps using several stages, whereby the solution at one stage is interpolated and fed as inflow condition to the next stage [51]. However, the use of very long domains may lead to unacceptable computational cost, which makes it certainly unsuitable for industrial problems, in which the development length shall be minimized. Several previous studies have therefore attempted to define an inflow length, namely the minimal distance from the inflow at which the flow properties become independent of the inflow forcing. This subject was dealt with regarding experiments [3], and regarding DNS data [28]. In the latter study, it was concluded that inflow effects tend to be concentrated in the wake region, but some effect is also observed in the near-wall region, with the conclusion that DNS data should be carefully scrutinized just like experiments. Schlatter and Örlü [29] investigated the effect of the influence of tripping on the development of a boundary layer with laminar inflow, concluding that tripping effects are mainly responsible for large spread of the numerical results. Wenzel et al. [43] attempted to extend the previous studies to compressible flows. By defining the inflow length based on fulfilment of mean momentum balance, those authors found that it increases monotonically with the free-stream Mach number, as also confirmed by Huang et al. [11]. The latter authors also noticed significant differences of numerical results obtained with the digital filtering (DF) and with the recycling/rescaling (RR) procedure, especially regarding the wake region. Adler et al. [1] and Dhamankar et al. [5] reported significant scatter across simulations with similar set-up and different inflow, concluding that the prediction of the wall properties is quite unreliable. Regardless of the turbulence seeding method, the inflow development length can be somewhat reduced by using sponge layers [16].

Given this background, it is clear that despite general acknowledgement, the problem of inflow effects on numerical simulations of high-speed wall-bounded flows is far from being quantitatively assessed. The goal of the present study is thus threefold. First, we aim at setting up a standardized procedure to evaluate achievement of equilibrium conditions in the numerical simulation of high-speed boundary layers. Second, and related to the previous item, we aim at developing a benchmark database to be used for the evaluation of the performance of inflow feeding techniques, which is devoid from inflow history effects, Third, we aim at developing improved versions of the most widely used inflow feeding techniques, namely the recycling–rescaling procedure [17,41,49] and the digital filtering procedure [14,39].

The paper is organized as follows: in Sect. 2, we provide generalities about turbulence seeding methods and suggest alternatives; in Sect. 3, we describe the numerical database, and in Sect. 4 we analyse the benchmark data set; the results of comparative tests with different inflow turbulence seeding are presented in Sect. 5, which serves as a basis for the estimation of the inflow length, as reported in Sect. 6.

2 Generating inflow turbulence

This study is focussed on the two most commonly used techniques for feeding inflow turbulence, namely the recycling/rescaling and the digital filtering procedure, and we discuss possible modifications. For later reference, all inflow properties (namely density ρ, velocity u_i and pressure p) are split into mean and fluctuating parts, namely

$$\begin{aligned} \rho(0,y,z,t) &= \bar{\rho}_0(y) + \rho_0'(y,z,t) \\ u_i(0,y,z,t) &= \tilde{u}_{i0}(y) + u_{i0}''(y,z,t) \\ p(0,y,z,t) &= \bar{p}_0 \end{aligned} \tag{1}$$

where 0 subscript is used to denote inflow quantities, overline and prime symbols denote ensemble-averaged quantities and fluctuations thereof, whereas tilde and double-prime symbols denote Favre-averaged properties and fluctuations thereof, e.g. $\tilde{\varphi} = \overline{\rho\varphi}/\bar{\rho}, \varphi'' = \varphi - \tilde{\varphi}$. Wall units, based on the friction velocity ($u_\tau = \sqrt{\tau_w/\rho_w}$, where τ_w is the wall shear stress), and the viscous length scale ($\delta_v = \mu_w/u_\tau/\rho_w$, with ρ_w and μ_w being the wall density and dynamic viscosity), will be denoted with the $+$ superscript. The forthcoming paragraphs deal with specification of inflow fluctuations aiming to mimic realistic turbulence.

2.1 The recycling/rescaling procedure

The procedure followed recycling/rescaling is sketched in Fig. 1. Following the original formulation of Lund et al. [17] and its compressible flow extension [49], the fluctuations of each flow variable are extracted at a suitable station (say x_r) and recycled to the inflow plane, after suitable rescaling.

The rescaling procedure is applied by dividing the boundary layer into two sub-layers: (i) the inner layer (superscript 'inn') where velocity is assumed to scale in wall coordinates ($y^+ = y/\delta_v$) ; and (ii) the outer layer (superscript 'out') where flow properties scale in outer units ($Y = y/\delta$, δ being the local boundary layer thickness). The fluctuation of a generic quantity (φ) is assumed to be a weighted combination of the inner- and outer-layer fluctuations

$$\varphi = \varphi^{\text{inn}}[1 - W(Y)] + \varphi^{\text{out}}\, W(Y), \tag{2}$$

where the weight function $W(Y)$ is defined as [17]

$$W(Y) = \frac{1}{2}\left\{1 + \tanh\left[\frac{\alpha(Y-b)}{(1-2b)Y+b}\right] \Big/ \tanh\alpha\right\}, \tag{3}$$

with $\alpha = 4, b = 0.2$. The inflow density and velocity fluctuations in each layer are rescaled from the recycling station according to

$$\begin{aligned} \rho_0'|^{\text{inn}}(y^+,z,t) &= \rho'(x_r, y^+, z + L_z/2, t), \\ u_{i0}''|^{\text{inn}}(y^+,z,t) &= \gamma\, u_i''(x_r, y^+, z + L_z/2, t), \\ \rho_0'|^{\text{out}}(Y,z,t) &= \rho'(x_r, Y, z + L_z/2, t), \\ u_{i0}''|^{\text{out}}(Y,z,t) &= \gamma\, u_i''(x_r, Y, z + L_z/2, t), \end{aligned} \tag{4}$$

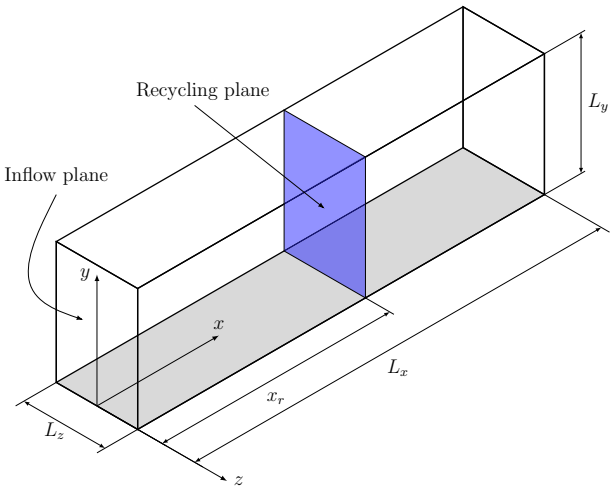

Fig. 1 Set-up for recycling/rescaling: x_r denotes the position of the recycling plane, and L_x, L_y and L_z denote the size of the computational box

where γ is the rescaling parameter, $\gamma = u_{\tau 0}/u_{\tau r}$, which we estimate as $\gamma = (\delta_r/\delta_0)^\kappa$, with $\kappa = 0.13$. The inflow conditions are softly enforced by carrying out characteristic decomposition at the computational boundary in which the incoming wave amplitudes are estimated from a target flow state [24], as defined in Eq. (4), with the additional assumption of uniform pressure.

To promote streamwise decorrelation, the inflow fluctuations at the spanwise location z are recycled from a staggered location $(z + L_z/2)$ at the recycling station [37], and random divergence-free disturbances with maximum amplitude $4\%\, u_0$ are added at the inflow to break any remaining symmetry. Following previous studies [22], the recycling station is placed at $x_r = 53\delta_0$. Preliminary simulations carried out by moving the recycling station to $x_r = 30\delta_0$ have shown negligible differences in the computed flow statistics. This baseline form of the recycling/rescaling procedure is hereafter referred to as RR1.

Possible simplifications of the RR procedure are also considered here. Instead of taking a linear combination of inner- and outer-rescaled fluctuations, one can more simply consider a remapping of the wall-normal coordinate with a stretching factor defined to be $\delta_{\nu,r}/\delta_{\nu,0}$ close to the wall (to achieve correct rescaling in the inner layer) and δ_r/δ_0 away from it (to achieve correct rescaling in the outer layer). Here, we consider a simple tanh blending of the type

$$\frac{\hat{y}}{y} = \frac{\delta_{\nu,0}}{\delta_{\nu,r}} + \frac{1 + \tanh\left[\log(Y/Y_c)/\Delta\right]}{2}\left(\frac{\delta_0}{\delta_r} - \frac{\delta_{\nu,0}}{\delta_{\nu,r}}\right), \tag{5}$$

where $Y_c = 0.08$ and $\Delta = 1.1$, the former defining the crossover between the inner and outer transformations, while the latter controlling the smoothness of the blending. The fluctuations at the inflow station are then obtained as follows:

$$\begin{aligned} \rho_0'(\hat{y}, z, t) &= \rho'(x_r, y, z + L_z/2, t) \\ u_{i\,0}''(\hat{y}, z, t) &= \gamma u_i''(x_r, y, z + L_z/2, t). \end{aligned} \tag{6}$$

This variant is hereafter referred to as RR2. Finally, we also consider a simple variant which includes remapping of the wall-normal coordinate based only on the ratio of the boundary layer thicknesses δ_r/δ_0 (hence, $\hat{y}/y = \delta_0/\delta_r$) and which is hereafter referred to as RR3.

It is noteworthy that recycling/rescaling procedures require specification of the mean flow distributions in (1). Different from the original formulation of Lund et al. [17], in which both mean flow and fluctuations are recycled, in the present RR implementation the inflow mean distributions are specified by the user and left unchanged during the simulation. In our experience, this approach prevents long-time numerical drift, thus accelerating statistical convergence. As a consequence, the inflow boundary layer thickness does not change in time, with the additional advantage that no continuous control of δ_r/δ_0 is needed.

2.2 The digital filtering procedure

The digital filtering implementation relies on an extension of the technique originally introduced by Klein et al. [14], which makes use of the strong Reynolds analogy (SRA) [39], as introduced by Kempf et al. [13]. Specifically, synthetic velocity fluctuations are first generated from a white noise sample, which is then filtered based on a sequence of one-dimensional convolutions, thus obtaining a correlated signal in space and time, with arbitrarily prescribable integral length and time scales. Different wall-normal distributions of the spanwise integral length scale (Λ_z) are assigned for each velocity component. Following Xie and Castro [48], two length scales are used for the inner ($\Lambda_{z,\mathrm{inn}}$) and for the outer ($\Lambda_{z,\mathrm{out}}$) wall layer, which are suitably blended to give

$$\Lambda_z(y) = \Lambda_{z,\mathrm{inn}} + (\Lambda_{z,\mathrm{out}} - \Lambda_{z,\mathrm{inn}})\frac{1 + \tanh\left[(y/\delta_0 - 0.2)/0.03\right]}{2}. \tag{7}$$

The use of two distinct length scales can potentially cause issues within the blending region, where eddies generated from digital filtering can be truncated. This potential problem is, however, not observed here as the Reynolds numbers are low enough that the outer length scale is selected throughout. Values of the integral length scales are reported for each velocity component in Table 1. As reported by Xie and Castro [48], the digital filtering technique has rather small sensitivity to variations in the integral length scales. The authors found that, for an incompressible channel flow, 50% change of Λ_y and Λ_z yields less than 10% change in the normal stresses, and less than 13% in the shear stress at a distance of $10\delta_0$ from the inflow.

Table 1 Spanwise and streamwise integral length scales used in DF implementation for the velocity components u', v', w'

Λ_i	u'	v'	w'
$\Lambda_{z,\mathrm{inn}}/\delta_{v,0}$	150	75	150
$\Lambda_{z,\mathrm{out}}/\delta_0$	0.4	0.3	0.4
Λ_x/δ_0	0.8	0.3	0.3

$\Lambda_{z,\mathrm{inn}}$ is the inner integral length scale, $\Lambda_{z,\mathrm{out}}$ is the outer integral length scale, and Λ_x is the streamwise length scale

The wall-normal integral length scales are then selected as $\Lambda_y(y) = 0.67\Lambda_z(y)$. Finally, constant values of the longitudinal integral length scales Λ_x are assigned for each velocity component as in Table 1. The streamwise length scales are then converted to time scales using Taylor hypothesis, assuming that eddies are convected at the free-stream velocity. The resulting velocity fluctuations are then rescaled to match a desired wall-normal distribution of Reynolds stresses. Temperature fluctuations T' are obtained by applying SRA (namely, $T' = -\tilde{u}u''/c_p$, where the tilde denotes Favre averages, and c_p is the specific heat at constant pressure), and converted to density fluctuations assuming zero pressure fluctuations. This baseline implementation of the DF algorithm is hereafter referred to as DF1.

Modifications of the baseline DF algorithm are also considered in the present work. In preliminary attempts of improving the performance of DF, we found that removing the streamwise velocity fluctuations at the inflow yields a reduction in spurious pressure disturbances generated by the DF1 implementation. This variant is referred to as DF2 in the following. A further improvement includes introducing a suitable stream function for the cross-stream velocity fluctuations to make the inflow turbulence solenoidal. The stream function is defined such as

$$v' = \frac{\partial \Psi'}{\partial z}, \quad w' = -\frac{\partial \Psi'}{\partial y}, \tag{8}$$

and we assume

$$\Psi'(y, z, t) = C(y)\, r(y, z, t), \tag{9}$$

where $r(y, z, t)$ is obtained from application of a low-pass filter to a white noise generator, and $C(y)$ is a suitable scaling function. The cross-stream velocity fluctuations are then obtained from Eq. (8). The shape of the scaling function is chosen so as to achieve a prescribed distribution of the wall-normal Reynolds stress,

$$\overline{v'v'} = \overline{\frac{\partial \Psi'}{\partial z}\frac{\partial \Psi'}{\partial z}} = C^2(y)\overline{\frac{\partial r}{\partial z}\frac{\partial r}{\partial z}}. \tag{10}$$

It is noteworthy that the variance term at the right-hand side of (10) can be computed beforehand, depending only on the spanwise length scale Λ_z in this formulation. As the present method hard enforces the distribution of the wall-normal velocity variance, the spanwise variance cannot be controlled independently to fit the target distribution. This variant is referred to as DF3 in the following.

It should be pointed out that various choices can be made to introduce the stream function Ψ. Whereas defining the stream function based on ρu_{i0} would allow us to find a flow field that has $\partial\rho/\partial t = 0$, defining the stream function based on u_{i0} helps us find a flow field that has zero dilatation. As the goal of the DF3 method is to minimize spurious acoustics, the second option is the most suitable one owing to the strong connection between dilatation and acoustics (while acoustic waves have nonzero $\partial\rho/\partial t$). In fact, regardless of how we define the stream function Ψ, a fully developed field has significant $\partial u/\partial x$, but small dilatation $\partial u_j/\partial x_j$, and thus Ψ is far from zero. This means that the DF3 inflow condition is not a good approximation of the corresponding fully developed flow field at the inflow location. However, combined with the choice of $u' = 0$, this approach produces a random incoming velocity field that has zero dilatation and thus small spurious acoustic waves.

3 The numerical database

Two reference flow cases have been selected, one representative of supersonic adiabatic boundary layers [22] and the other of hypersonic cooled boundary layers [51]. The former work refers to free-stream Mach number

Table 2 Summary of DNS flow cases

Flow case	M_0	Re_{δ_0}	L_x/δ_0	L_y/δ_0	L_z/δ_0	L_z/δ_f	Δx^+	Δy_w^+	Δz^+	$N_x \times N_y \times N_z$
M2-RR	2.00	12,662	106	8.3	9.6	3.6	6.4	0.6	5.4	$4160 \times 221 \times 448$
M2-DF	2.00	12,662	159	8.3	9.6	3.0	6.4	0.6	5.4	$6240 \times 221 \times 448$
M2-L1	2.00	4779	310	26	32	6.4	4.3	0.6	4.4	$6144 \times 512 \times 768$
M2-L2	2.00	8230	310	26	26	5	4.2	0.6	4.0	$10{,}240 \times 512 \times 896$
M2-L3	2.00	12,662	318	16.6	19.2	3.3	5.3	0.6	4.4	$12{,}480 \times 448 \times 896$
M5.84-RR	5.84	23,152	150	10	9	2.8	8.9	0.4	8.4	$5024 \times 224 \times 320$
M5.84-DF	5.84	23,152	150	10	9	2.8	8.9	0.4	8.4	$5024 \times 224 \times 320$
M5.84-L1	5.84	10,650	300	20	18	3.7	3.5	0.4	3.3	$10{,}048 \times 352 \times 640$
M5.84-L2	5.84	16,788	300	20	18	3.6	5.2	0.4	4.9	$10{,}048 \times 352 \times 640$
M5.84-L3	5.84	23,152	300	20	18	3.1	7.1	0.4	6.7	$10{,}048 \times 352 \times 640$

The suffix RR denotes cases run with the recycling–rescaling procedure, and DF denotes cases run with the digital filtering procedure. The suffix L denotes benchmark simulations, run in long domains. M_0 is the free-stream Mach number, $Re_{\delta_0} = \rho_0 u_0 \delta_0/\mu_0$ is the Reynolds number based on the inflow boundary layer thickness, L_x, L_y, L_z are the domain streamwise, wall-normal and spanwise sizes, Δx^+, Δz^+ are the grid spacings in the wall-parallel direction, Δy_w^+ is the minimum wall-normal grid spacing, and N_x, N_y, N_z are the number of grid points, and δ_f is the outflow boundary layer thickness

$M_0 = 2$ and nominally adiabatic wall conditions ($T_w = T_r = 1 + r(\gamma - 1)/2M_0^2$, where $r = Pr^{1/3}$ is the recovery factor and $Pr = 0.72$ the Prandtl number), and the latter has $M_0 = 5.84$, $T_w/T_r = 0.25$.

All simulations are carried out using a GPU-accelerated solver [2], which combines the energy-preserving properties of a sixth-order skew-symmetric central difference scheme [20] with the shock-capturing properties of a fifth-order weighted essentially non-oscillatory (WENO) scheme, through a modified Ducros shock sensor [21]. The sensor is disabled for the supersonic flow cases, whereas we have found that, although the flow does not include shocks, minimal numerical dissipation provided by WENO is needed for stability in the hypersonic flow cases. In all simulations, the diffusive fluxes are discretized with sixth-order central formulas, and time integration is carried out using a third-order Runge–Kutta method [46].

For both flow cases under scrutiny, two series of DNS have been carried out, one on relatively short domains, which serve to quantify effects of inflow seeding (RR- or DF-type), as compared to benchmark simulations, carried out in very long domains, which are verified to be yield to a healthy state of developed turbulence. The full list of DNS and the key computational parameters are reported in Table 2.

The supersonic data set includes six DNS in short domains and three DNS in long domains. All cases with RR seeding share the same mesh, which is identical to that used by Pirozzoli and Bernardini [22], whereas cases with DF feeding use a 50% longer mesh to reach comparable Reynolds number. In the short-domain simulations, the mean flow properties (as well as the turbulent stresses needed in DF) are taken from Pirozzoli and Bernardini [22]. The mean profiles for the long-domain DNS have instead been determined by applying the Van Driest transformation [36] to boundary layer profiles of the Musker family [19]. The hypersonic data set includes four DNS in short domains, and three in long domains. The choice of the inflow mean profiles is crucial in this case, as the Van Driest transformation is known to be inaccurate in the case of cold walls [40,51], and to perform poorly in the wake part of the wall layer, even under adiabatic conditions [44]. Hence, the inflow mean profiles for the M5.84-L1 RR simulation have been extracted from a coarser precursor DNS, and the simulation is used to provide mean inflow profiles for the other DNS. We note that the DF2 inflow condition is not considered for hypersonic cases as it fails to yield sustained turbulence. RR3 feeding is also disregarded as found to provide similar performance to RR1 in supersonic cases.

The statistical properties of the boundary layers are hereafter reported in terms of either standard or density-weighted (Favre) averages. Time averages are denoted as $\bar{f}$, whereas Favre averages are defined as $\tilde{f} = \overline{\rho f}/\bar{\rho}$, with double primes denoting fluctuations thereof, $f'' = f - \tilde{f}$. For the short-domain simulations, time averages are accumulated over at least 800 and 1750 convective time units (δ_0/u_0), for the $M_0 = 2$ and $M_0 = 5.84$ flow cases, respectively, taking advantage of spanwise averaging.

For the long-domain simulations, at least 1450 and 1750 convective time units have been used, respectively. Time averaging is initiated after a statistically homogeneous condition is reached, as inferred by monitoring the evolution of the spanwise-averaged wall properties. For all computations, spatially developing boundary layers, based on superposing van Driest-transformed velocity profiles with organized eddies resulting from the digital filtering procedure, are used as initial conditions.

For later guidance in the interpretation of the results, the distributions of the friction and momentum thickness Reynolds numbers for DNS in short domains are reported in Fig. 2, which makes it clear that

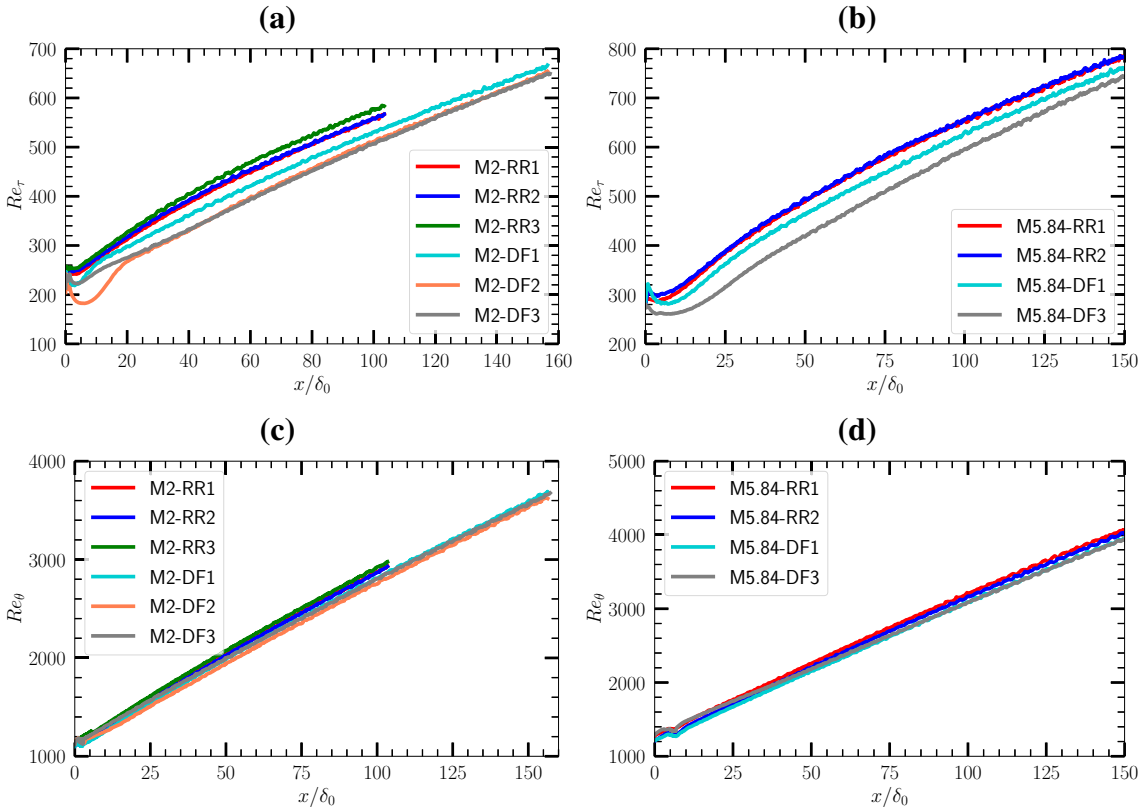

Fig. 2 Streamwise distribution of Re_τ (**a**, **b**) and Re_θ (**c**, **d**) with RR and DF inflow seeding, for supersonic (**a**, **c**) and hypersonic (**b**, **d**) flow cases

different behaviours are obtained depending on the inflow seeding technique, and which are most evident in Re_τ, whereas Re_θ is much more weakly affected.

4 Results of benchmark simulations

A mandatory step for the evaluation of inflow turbulence feeding methods is the establishment of high-fidelity scaling laws for the main quantities of interest, as turbulence statistics, wall friction and heat transfer. This is of course important in its own sake for use in engineering analyses. In this respect, the first step is the identification of one or several diagnostic parameters, which allow to ascertain that an equilibrium turbulence state is achieved. The first diagnostic implies fulfilment of mean momentum balance [36],

$$\begin{aligned} \overline{\rho}\tilde{u}\frac{\partial \tilde{u}}{\partial x} + \overline{\rho}\tilde{v}\frac{\partial \tilde{u}}{\partial y} &= -\frac{\partial \overline{p}}{\partial x} - \frac{\partial(\overline{\rho}\widetilde{u''u''})}{\partial x} + \frac{\partial(\overline{\sigma}_{xy} - \overline{\rho}\widetilde{u''v''})}{\partial y}, \\ 0 &= -\frac{\partial \overline{p}}{\partial y} - \frac{\partial(\overline{\rho}\widetilde{v''v''})}{\partial y}, \end{aligned} \tag{11}$$

where $\sigma_{xy} = \mu(\partial u/\partial y + \partial v/\partial x)$, and in which we have retained the normal Reynolds stresses $\widetilde{u''u''}$ and $\widetilde{v''v''}$, the latter possibly being relevant at high Mach number [10].

Wall-normal integration of Eq. (11), combined with the continuity equation and the assumption of zero external pressure gradient, leads to the compressible equivalent of the von Kármán equation, originally derived for incompressible flow [27],

$$\frac{C_f}{2} = \frac{\mathrm{d}\theta}{\mathrm{d}x} + \frac{1}{\rho_0 u_0^2}\frac{\mathrm{d}}{\mathrm{d}x}\int_0^\delta \bar{\rho}(\widetilde{v''v''} - \widetilde{u''u''})\mathrm{d}y, \tag{12}$$

where

$$\theta = \int_0^\delta \frac{\bar{\rho}\tilde{u}}{\rho_0 u_0}\left(1 - \frac{\tilde{u}}{u_0}\right)\mathrm{d}y,$$

is the momentum boundary layer thickness and $C_f = 2\tau_w/(\rho_0 u_0^2)$ is the friction coefficient. Equation (12) also includes a term depending on the streamwise variation of the turbulent stresses. It can be assumed that an equilibrium state is reached if the residual of Eq. (12) is smaller than a certain prescribed tolerance [11,30,43]. We thus define a relative error in this metric as

$$E_{\mathrm{VK}} = \frac{C_f/2 - \mathrm{d}\hat{\theta}/\mathrm{d}x}{C_f/2}, \tag{13}$$

where

$$\hat{\theta} = \theta + \frac{1}{\rho_0 u_0^2}\int_0^\delta \bar{\rho}(\widetilde{v''v''} - \widetilde{u''u''})\mathrm{d}y.$$

Two additional metrics refer to the development of the peaks of the turbulent shear stress, $\tau_{xy}^{\mathrm{pk}} = \max_y(-\overline{\rho}\widetilde{u''v''}/\tau_w)$, and of the streamwise velocity variance, $\tau_{xx}^{\mathrm{pk}} = \max_y(\overline{\rho}\widetilde{u''u''}/\tau_w)$. Correlations for the peak turbulent shear stress were suggested by Chen et al. [4]

$$\tau_{xy}^{\mathrm{pk}} = 1 - B_1 Re_\tau^{-6/7}, \tag{14}$$

with $B_1 = 13.7$ for incompressible flow. As regards the streamwise velocity variance, Pirozzoli and Bernardini [23] found it grows logarithmically with Re_τ,

$$\tau_{xx}^{\mathrm{pk}} = A_2 + B_2 \log Re_\tau, \tag{15}$$

with $A_2 = 3.35$ and $B_2 = 0.725$. Two obvious additional diagnostic parameters include the friction coefficient (C_f) and the heat transfer coefficient,

$$C_h = \frac{q_w}{\rho_0 u_0 C_p (T_w - T_r)} \tag{16}$$

where $q_w = k\partial T/\partial y|_w$ is the wall heat flux, with $k = \mu/(Pr\, C_p)$ the thermal conductivity. Power-law relationships versus Re_θ are generally assumed for these parameters, namely

$$C_f = A_3 Re_\theta^{-B_3}, \quad C_h = A_5 Re_\theta^{-B_5}, \tag{17}$$

where $A_3 = 0.024$ and $B_3 = 0.25$ for incompressible flow [35]. Finally, we consider the wall pressure variance, which is relevant in aero-vibroacoustic analysis. As shown by Jiménez et al. [12] and Pirozzoli and Bernardini [22], this quantity also includes contributions from distant eddies residing in the outer layer, hence incomplete boundary layer development may reflect into inaccurate prediction of this indicator. Farabee and Casarella [9] found a convenient representation in the form,

$$\overline{p_w'^2}^+ = A_4 + B_4 \log Re_\tau, \tag{18}$$

with $A_4 = -4.30$, $B_4 = 1.86$ for incompressible flow.

4.1 Supersonic benchmark flow cases

Figure 3 shows the distribution of the relative error in mean momentum balance, as defined in (13), for the three benchmark simulations in long domains. Large errors are found close to the inflow, similar to what reported by Schlatter et al. [30] for a incompressible boundary layers. In fact, the metric (13) provides a measure for the degree of development of a boundary layer in terms of its adherence to the thin-shear-layer equations [36]. Therefore, each neglected term in Eq. (12) can in principle be responsible of the observed imbalance. Momentum balance is satisfied to within 1% error only at a distance of about $100\delta_0$. For further safety margin, we only consider the last third part of the domain to develop reference correlation laws for the various diagnostic quantities.

The peak shear stress is considered next in Fig. 4a. The DNS data support validity of Eq. (14), with $B_1 = 13.62$, which is in remarkable agreement with what reported by Chen et al. [4]. Hence, it appears that density scaling is quite effective in mapping this particular metric from adiabatic boundary layers into their incompressible counterparts. The streamwise evolution of the peak streamwise velocity variance shown in Fig. 4 very well conforms with Eq. (15), with $A_2 = 3.35$, $B_2 = 0.725$ [23]. Figure 4 also reports the results obtained by Wenzel et al. [45], with corresponding best fits. Slight underprediction of both the pressure variance and the turbulent shear stress peak is generally found, as compared to the present data. Nonetheless, their results fall within a $\pm 2\%$ uncertainty band from our inferred trends. On account of the different numerical approaches involved, the agreement is quite good.

Regarding the friction relation, Fig. 5a shows that the benchmark simulations follow Eq. (17) quite well, with fitting coefficients $A_3 = 0.0174$, $B_3 = 0.245$. Last, the pressure variance shown in Fig. 5b follows

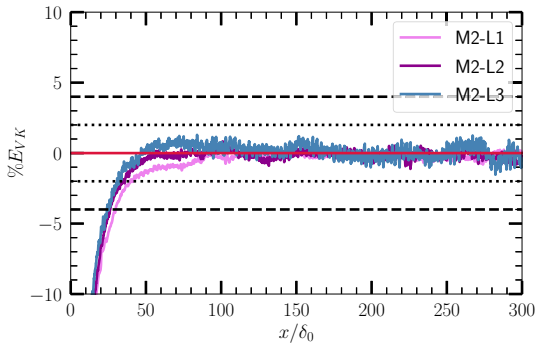

Fig. 3 Supersonic boundary layer benchmark flow cases: streamwise distributions of relative error in mean momentum balance. Solid lines denote the DNS data, dashed lines denote a $\pm 4\%$ error band, and dotted lines denote a $\pm 2\%$ error band

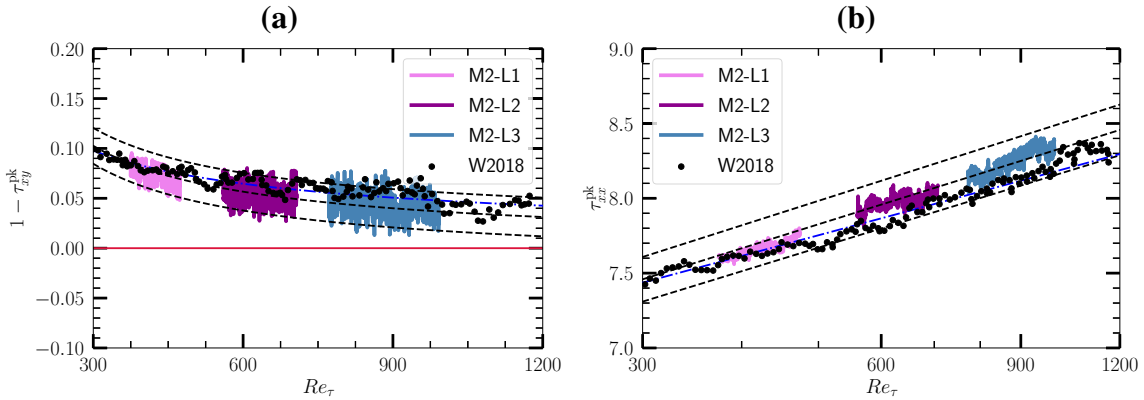

Fig. 4 Supersonic boundary layer benchmark flow cases: distribution of turbulent shear stress peak (**a**) and of peak streamwise velocity variance (**b**) as a function of friction Reynolds number. Coloured solid lines denote DNS data, and the black circles denote data of Wenzel et al. [45]. The dashed line in panel (**a**) denotes Eq. (14) and a $\pm 2\%$ uncertainty band. The dashed line in panel (**b**) denotes Eq. (15) and a $\pm 2\%$ uncertainty band. Blue dash-dotted lines denote data fits for Wenzel et al. [45] (colour figure online)

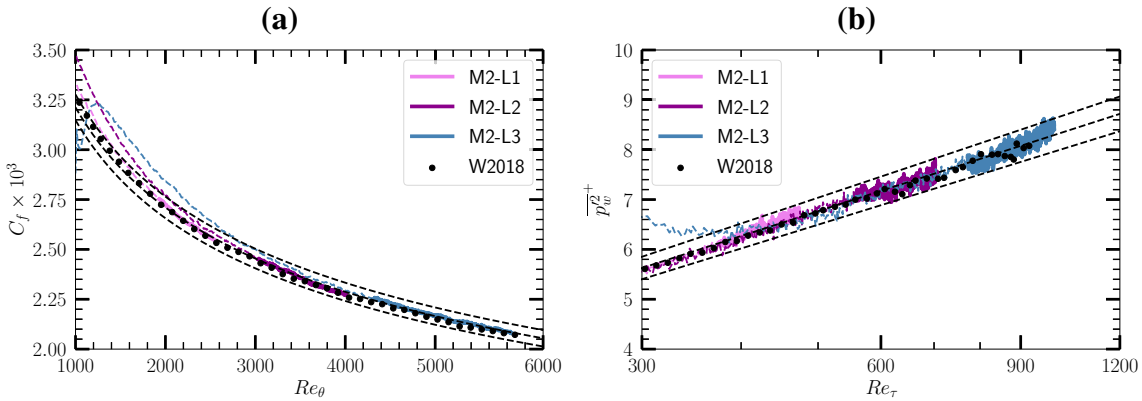

Fig. 5 Supersonic boundary layer benchmark flow cases: distribution of friction coefficient as a function of momentum thickness Reynolds number (**a**), and of wall pressure variance as a function of friction Reynolds number (**b**). Coloured lines denote the present DNS results taken in the first two-thirds of the domain (dashed lines), and in the last third (solid lines). Black circles denote data of Wenzel et al. [45]. The dashed black lines in panel (**a**) denote the reference correlation (17) and a $\pm 2\%$ uncertainty band. The dashed black lines in panel (**b**) denote the reference correlation (18) and a $\pm 4\%$ uncertainty band (colour figure online)

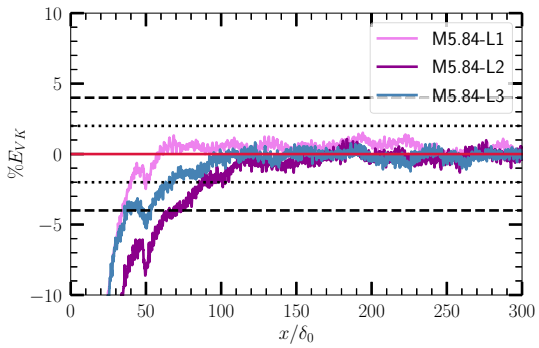

Fig. 6 Hypersonic boundary layer benchmark flow cases: streamwise distributions of relative error in mean momentum balance. Solid lines denote the DNS data, dashed lines denote a $\pm 4\%$ error band, and dotted lines denote a $\pm 2\%$ error band

Eq. (18), with fitting coefficients $A_4 = -7.09$, $B_4 = 2.23$. Almost perfect agreement is observed between these correlations, and trends found by Wenzel et al. [45], throughout the Reynolds number range.

4.2 Hypersonic benchmark flow cases

Fulfilment of the von Kármán integral equation for the benchmark hypersonic flow cases is verified in Fig. 6, which shows longer inflow length as compared to the supersonic cases. In fact, about $35 - 70\delta_0$ are needed in order to fall within the 4% accuracy band. This finding is consistent with previous results of Huang et al. [11] and Wenzel et al. [43], who reported a monotonic increase in the inflow length with the free-stream Mach number. We additionally find that DNS with higher inflow Reynolds number require longer distance to adjust.

The peak shear stress and the wall pressure variance are shown in Fig. 7a. As for the supersonic case, the shear stress peak still varies approximately as given in by Eq. (14), with $B_1 = 29.8$. The wall pressure variance still exhibits logarithmic increase with Re_τ as predicted by Eq. (18), with $A_4 = 3.37$ and $B_4 = 1.32$, hence the growth is slower than in the supersonic case. The pressure variance is larger than in the supersonic case, as the result of finite heat transfer at the wall, as previously noticed by Huang et al. [11] and Zhang et al. [50].

The two most important flow properties in the study of hypersonic flow are obviously the friction coefficient and the wall heat transfer coefficient, which are reported in Fig. 8. A power-law dependence on Re_θ is assumed as in equation (17), which yields the fitting constants $A_3 = 0.0131$, $B_3 = 0.268$, $A_5 = 0.00774$, $B_5 = 0.272$. Hence, the decay of C_f is a bit steeper than in the supersonic case. All the fitting coefficients in equations (14)-(18) are listed for convenience in Table 3.

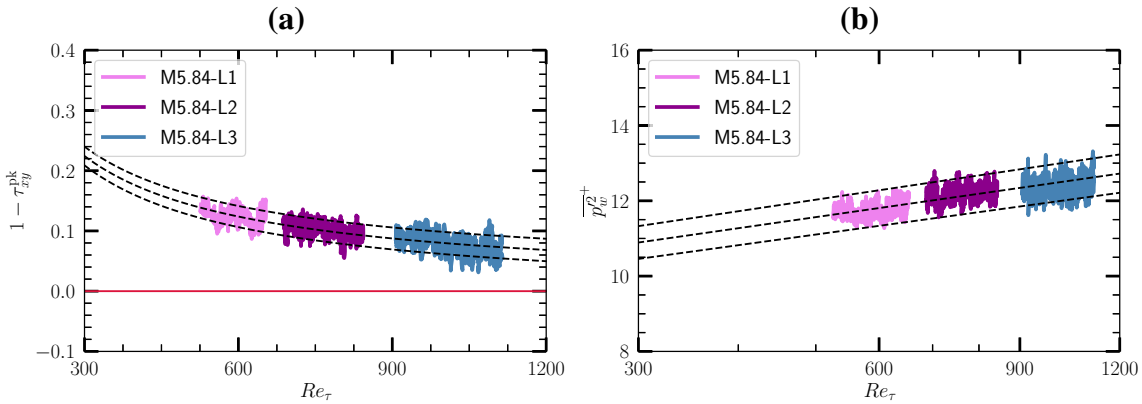

Fig. 7 Hypersonic boundary layer benchmark flow cases: distribution of turbulent shear stress peak (**a**) and of wall pressure variance (**b**) as a function of friction Reynolds number. Solid coloured lines denote DNS data. The black dashed lines in panel (**a**) denote Eq. (14) with a $\pm 2\%$ error band. The black dashed lines in panel (**b**) denote Eq. (18) and a $\pm 4\%$ error band (colour figure online)

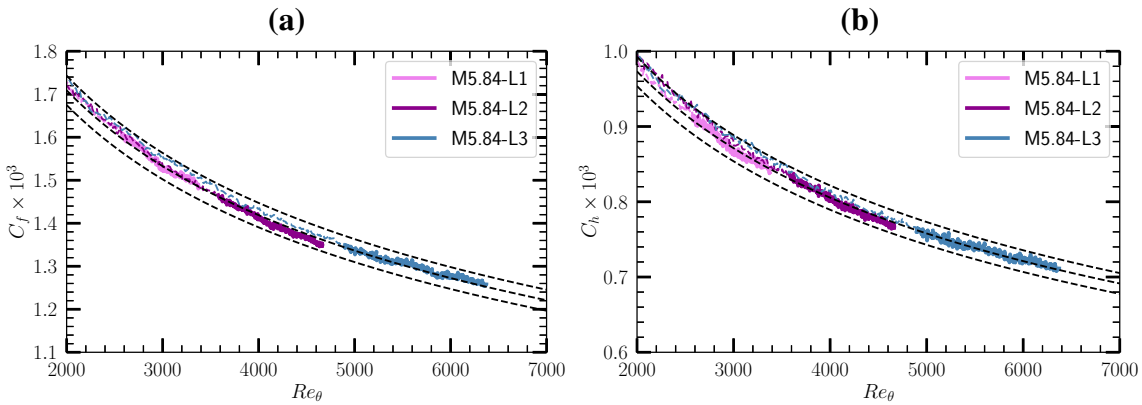

Fig. 8 Hypersonic boundary layer benchmark flow cases: distributions of wall friction coefficient (**a**) and of heat transfer coefficient (**b**) as a function of momentum thickness Reynolds number. Coloured lines denote the present DNS results taken in the first two-thirds of the domain (dashed lines), and in the last third (solid lines). The dashed black lines in panels (**a**, **b**) denote the reference correlations (17) and a $\pm 2\%$ uncertainty band (colour figure online)

Table 3 List of fitting coefficients in equations (14)–(18), as derived from supersonic and hypersonic benchmark DNS

Fit coefficients	Supersonic benchmark	Hypersonic benchmark
B_1	13.62	29.8
A_2, B_2	3.35, 0.725	–
A_3, B_3	0.0174, 0.245	0.0131, 0.268
A_4, B_4	−7.09, 2.23	3.37, 1.32
A_5, B_5	–	0.00774, 0.272

5 Effect of inflow turbulence seeding

Data from DNS in short domains are shown here, with the goal of evaluating the influence of the inflow seeding technique on the establishment of an equilibrium turbulence state, using the correlations established in the previous paragraphs as a benchmark.

5.1 Supersonic flow cases

Figure 9 shows the distribution of the relative error in von Kármán equation for supersonic flow cases in relatively short domains. All DNS fall inside the 4% error band past at a distance 10-25δ_0 from the inflow.

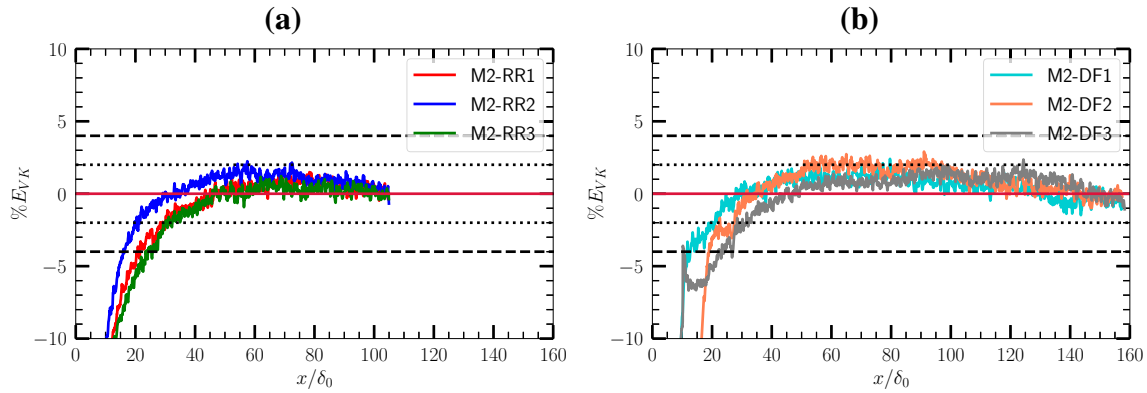

Fig. 9 Supersonic flow cases: streamwise distributions of relative error in mean momentum balance. The solid lines denote DNS data using RR inflow (**a**) and DF inflow (**b**); the dashed and the dotted lines denote $\pm 4\%$ and $\pm 2\%$ error bands, respectively

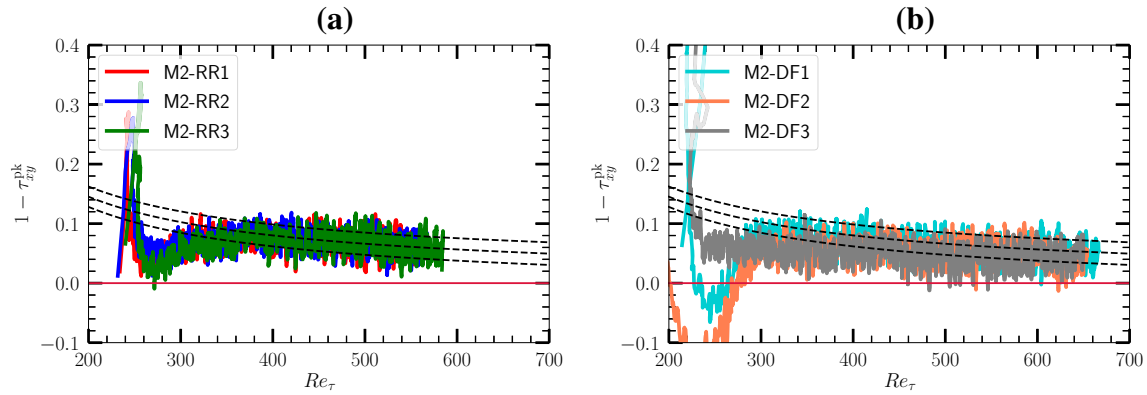

Fig. 10 Supersonic flow cases: distributions of peak turbulent shear stress as a function of friction Reynolds number. The solid lines denote DNS data using RR inflow (**a**) and DF inflow (**b**); the dashed lines denote depict reference distributions obtained from the benchmark DNS and a $\pm 2\%$ error band

Past this point, some scatter across curves is found, with RR generally performing better than DF, in that it yields smaller error for given distance from the inflow. No systematic differences are observed among different implementations of the two techniques.

Figure 10 shows the distributions of the peak turbulent shear stress, which highlights some differences among the various approaches. Whereas the shear stress peak never exceeds unity in all DNS with RR, the DF1 and the DF2 cases exceed this threshold in a large region near the inflow, which makes the flow statistics quite unphysical. On the other hand, the DF3 implementation yields results more similar to RR, and quicker adjustment to equilibrium. The peak shear stress appears to monotonically approach unity at $Re_\tau \approx 400$, but careful inspection of the figure suggests that DF tends to overestimate the trends returned from the benchmark DNS (dashed line), and to occasionally exceed unity.

The peak streamwise velocity variance is shown in Fig. 11. Notably, the DF has a more benign behaviour regarding this variable, as all DF implementations attain the correct behaviour at $Re_\tau \gtrsim 300$, despite large excursions from the reference trends in the initial transient. On the other hand, values in excess of $Re_\tau = 400$ are needed for RR statistics to fall within the $\pm 2\%$ error band. As a result, RR requires longer fetch ($x/\delta_0 \approx 80$) for proper development of the streamwise turbulent stress.

The DF technique also appears to perform better than RR as regards the prediction of the friction coefficient, as shown in Fig. 12. In fact, despite much smoother initial transient, RR tends to consistently overpredict C_f, with values falling within $\pm 2\%$ error only at $Re_\theta \gtrsim 3000$, corresponding to the end of the computational domain employed for these DNS. The results of all RR-based DNS are quite similar, meaning that implementation details are unimportant in the observed behaviour. Despite substantial differences in the inflow recovery region, all DF implementations yield a C_f within a $\pm 2\%$ error band at $Re_\theta \gtrsim 2000$, i.e. at $x/\delta_0 \gtrsim 50$, and basically landing on the benchmark distribution at $Re_\theta \approx 3000$. The DF3 implementation seems to be a bit slower

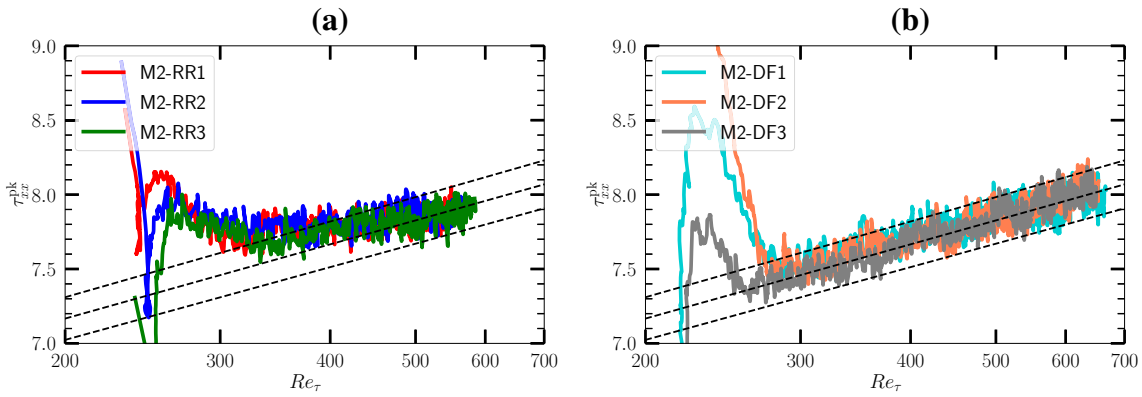

Fig. 11 Supersonic flow cases: distributions of peak streamwise turbulent stress as a function of friction Reynolds number. The solid lines denote DNS data using RR inflow (**a**) and DF inflow (**b**); the dashed lines denote reference distributions obtained from the benchmark DNS, and a $\pm 2\%$ error band

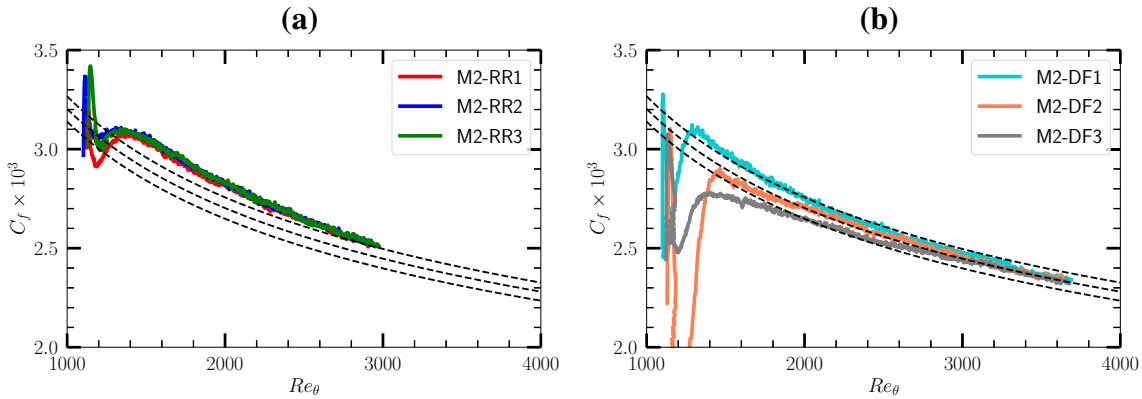

Fig. 12 Supersonic flow cases: distributions of friction coefficient as a function of momentum thickness Reynolds number. The solid lines denote DNS data using RR inflow (**a**) and DF inflow (**b**); the dashed lines denote reference distributions obtained from the benchmark DNS, and a $\pm 2\%$ error band

than the other in this respect. It is noteworthy that the strong dips next to the inflow section seen in the DF simulations could in principle be mitigated as suggested by Larsson [16].

The von Kármán equation (12) can be used to connect observations made regarding the friction coefficient and the peak streamwise turbulent stress. In fact, Fig. 12 highlights irregular distribution of C_f next to the inflow in the DF simulations, with sharp increase, followed by abrupt drop. The von Kármán equation clarifies that those regions are connected with u' fluctuations, as the initial increase in the momentum flux deficit (namely $\mathrm{d}\theta/\mathrm{d}x$) and decrease in wall shear stress compensate the growth of the streamwise stress. This mechanism is reversed in the ensuing region, featuring strong reduction in the streamwise stress an growth of the wall shear stress.

The distributions of the wall pressure variance are shown in Fig. 13. All RR implementations exhibit roughly similar behaviour, as they achieve a monotonically increasing trend compatible with theory [9,22] and with the benchmark distribution at $Re_\tau \gtrsim 450$ (namely $x/\delta_0 \gtrsim 60$). The behaviour of the DF-based DNS is richer as different trends are found depending on the implementation details. In fact, the baseline DF1 implementation largely overpredicts pressure fluctuations, throughout the computational domain. This large disagreement is partially cured through suppression of the streamwise velocity fluctuations in the DF2 implementation, and even more by making the inflow cross-stream velocity divergence-free, as in the DF3 implementation. Both DF2 and DF3 indeed exhibit reasonably correct trends at $Re_\tau \gtrsim 300$ and $Re_\tau \gtrsim 400$, respectively, which is in line if not better than for the RR cases. Still, some consistent overprediction of pressure disturbances in the developed region is observable, which we interpret as the result of acoustic disturbances arising at the inlet owing to the unrealistic structure of the inflow velocity fluctuations.

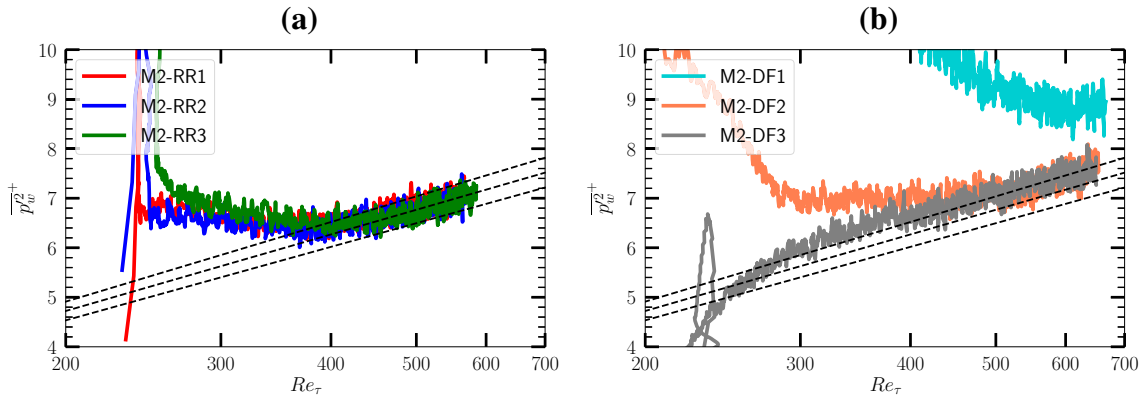

Fig. 13 Supersonic flow cases: distributions of wall pressure variance as a function of friction Reynolds number. Solid lines denote DNS data using RR inflow (**a**) and DF inflow (**b**); the dashed lines denote reference distributions obtained from the benchmark DNS, and a $\pm 4\%$ error band

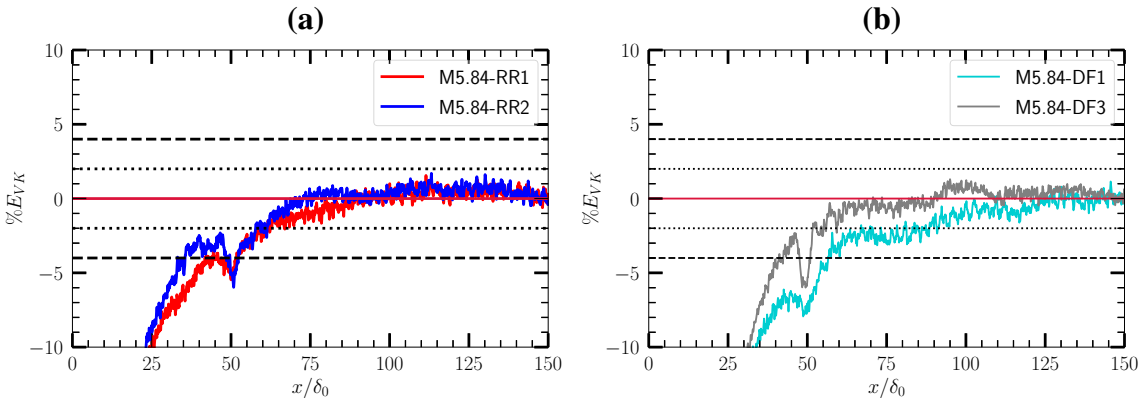

Fig. 14 Hypersonic flow cases: streamwise distributions of error in mean momentum balance. The solid lines denote DNS data using RR inflow (**a**) and DF inflow (**b**); the dashed and dotted lines denote a $\pm 4\%$ and $\pm 2\%$ error band, respectively

5.2 Hypersonic flow cases

Figure 14 shows the relative error for the von Kármán equilibrium condition for the RR (left panel) and DF (right panel) techniques. The two RR implementations herein considered have quite similar behaviour, with $\pm 4\%$ error band attained at $x \gtrsim 50\delta_0$, and the stricter threshold $\pm 2\%$ is reached at $x \gtrsim 60\delta_0$. Regarding DF cases, the baseline DF1 implementation is slower to adjust towards zero error, whereas the DF3 implementation (suppression of u' and stream function formulation) readjusts more quickly, falling within the $\pm 2\%$ error band quite early ($x \gtrsim 50\delta_0$). The peak turbulent shear stress is shown in Fig. 15, as a function of the friction Reynolds number. Unlike the supersonic cases, the peaks for both RR and DF cases remain strictly below unity, throughout the computational domain. Near equilibrium conditions are reached for $Re_\tau \gtrsim 500$ (corresponding to $x \approx 55\delta_0$ for RR1, RR2, DF1 and $x \approx 75\delta_0$ for DF3). At higher Re, the RR cases consistently follow the benchmark correlation, as the DF1 case also does. On the other hand the DF3 method seems to exhibit a plateau, followed by decline at $Re_\tau \gtrsim 600$ (corresponding to $x \approx 100\delta_0$). Figures 16 and 17 show the distributions of the friction coefficient and the heat transfer coefficient as a function of the momentum thickness Reynolds number. Not surprisingly, the two quantities exhibit a similar behaviour. We find that RR inflow feeding yields results which, past an initial dip, fall quite rapidly within the $\pm 2\%$ error band. The dip is found to be much larger when DF is used. However, as also found for the shear stress, the baseline DF1 implementation adjusts quite quickly at $Re_\theta \approx 2000$ similar to the RR cases, whereas the DF3 implementation requires longer fetch to reach equilibrium, at $Re_\theta \gtrsim 3000$ (corresponding to $x \gtrsim 95\delta_0$). In Fig. 18, we finally consider the wall pressure variance. Regarding this parameter, the RR method is capable of attaining a monotonically increasing trend with the Reynolds number at $Re_\tau \gtrsim 600$ (corresponding to $x \gtrsim 80\delta_0$); hence, the inflow adjustment length is much more than for supersonic cases. Past that location the data are in fair agreement with the

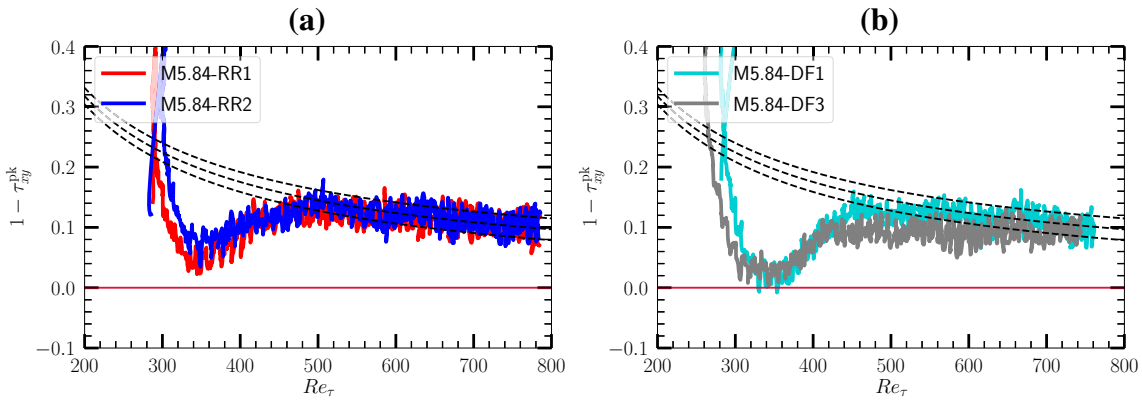

Fig. 15 Hypersonic flow cases: distributions of peak turbulent shear stress as a function of friction Reynolds number. The solid lines denote DNS data using RR inflow (**a**) and DF inflow (**b**); the dashed lines denote depict reference distributions obtained from the benchmark DNS and a $\pm 2\%$ error band

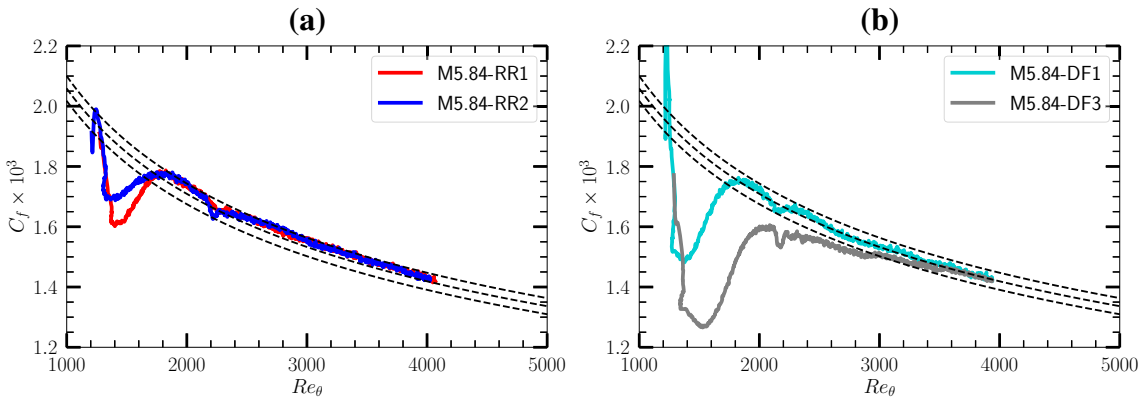

Fig. 16 Hypersonic flow cases: distributions of friction coefficient as a function of momentum thickness Reynolds number. The solid lines denote DNS data using RR inflow (**a**) and DF inflow (**b**); the dashed lines denote reference distributions obtained from the benchmark DNS, and a $\pm 2\%$ error band

benchmark correlation. The DF seeding exhibits results similar to the supersonic case. Whereas the baseline DF1 implementation starts from very large values and it tends to adjust to the expected behaviour towards the end of the computational domain, the use of solenoidal inflow fluctuations in the DF3 implementation yields a realistic behaviour starting much closer to the inflow ($Re_\tau \gtrsim 350$, corresponding to $x \gtrsim 30\delta_0$). In any case, pressure fluctuations in the developed region appear to be a bit larger than expected, thus corroborating the notion that the DF technique is inherently more noisy than RR.

6 Discussion and conclusions

We next attempt to draw a quantitative comparison of the predictive capabilities of the various inflow turbulence seeding techniques in terms of achieving accurate representation of a state of fully developed turbulence. For that purpose, in Figs. 19 and 20 we show, for each diagnostic parameter herein identified, the inflow distance needed to target the benchmark correlations previously determined to a given accuracy. For the sake of the present analysis, the flow statistics shown in the previous sections have been smoothed by using a Savitzky–Golay causal filter.

Inspecting the results of supersonic DNS in Fig. 19, one may infer that DF turbulence seeding is capable of achieving faster adaptation of the friction coefficient than RR. In fact, all DF implementations achieve $\pm 2\%$ confidence within $80\delta_0$ from the inflow, with DF2 substantially faster, with inflow length of about $30\delta_0$. RR feeding does not seem to reach the same level of accuracy within the selected computational domain, the error on friction being still 2% error at $100\delta_0$. The same error is obtained by all RR implementations, which also exhibit

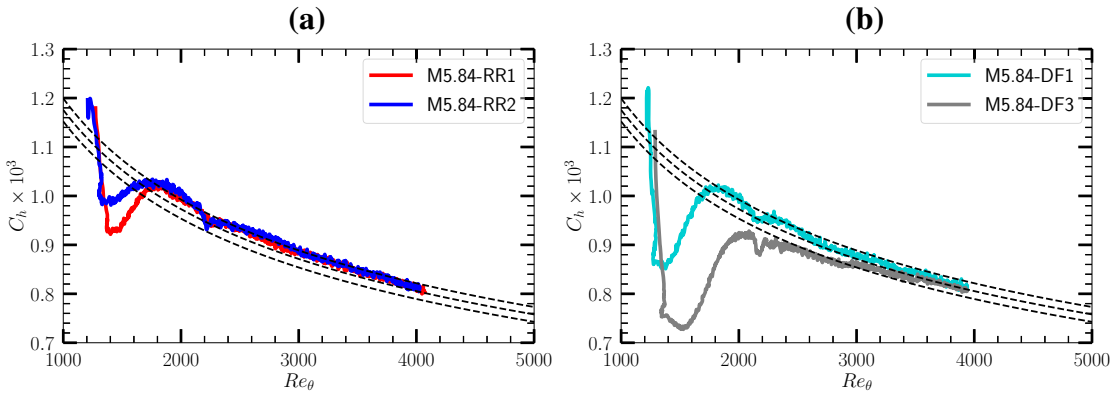

Fig. 17 Hypersonic flow cases: distributions of heat transfer coefficient as a function of momentum thickness Reynolds number. The solid lines denote DNS data using RR inflow (**a**) and DF inflow (**b**); the dashed lines denote reference distributions obtained from the benchmark DNS, and a $\pm 2\%$ error band

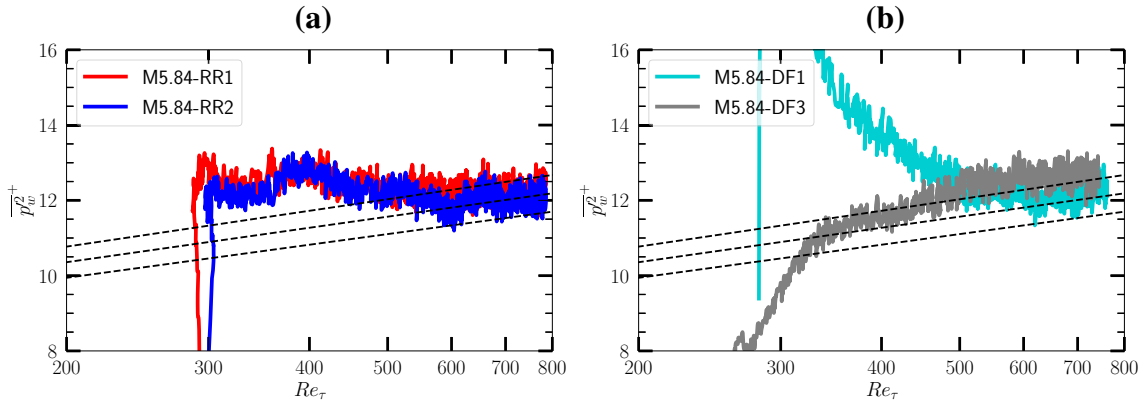

Fig. 18 Hypersonic flow cases: distributions of wall pressure variance as a function of friction Reynolds number. Solid lines denote DNS data using RR inflow (**a**) and DF inflow (**b**); the dashed lines denote reference distributions obtained from the benchmark DNS, and a $\pm 4\%$ error band

very similar trends. Regarding the peak streamwise velocity variance stress, one can likewise conclude that the DF1 and DF3 implementations are marginally better than RR. The DF2 case is obviously disadvantaged in this respect, as it has the lowest inflow turbulence kinetic energy. This criterion is, however, not very restrictive, as all RR and DF simulations require at most $40\delta_0$ to achieve $\pm 2\%$ accuracy. The wall pressure variance exhibits quite a different behaviour. In fact, whereas RR shows consistent convergence towards the reference equilibrium value, DF in its variants consistently overpredicts this property. Improvements over baseline DF1 are obtained from formulations DF2 and DF3, which nevertheless require an inflow length of about $100\delta_0$ to achieve 5% accuracy. Proposed variants of the RR technique (mainly the RR2 implementation) yield small but observable improvement in this metric as may be argued upon close inspection of Fig. 13a. Reducing the intensity of streamwise turbulent fluctuation intensity of DF thus yields beneficial effects on the wall pressure variance, but on the other hand it yields poorer prediction of the peak turbulent shear stress. As a result, at least $60\delta_0$ are required to achieve 3% error in this quantity, whereas DF1 and all RR implementations require $30\delta_0$

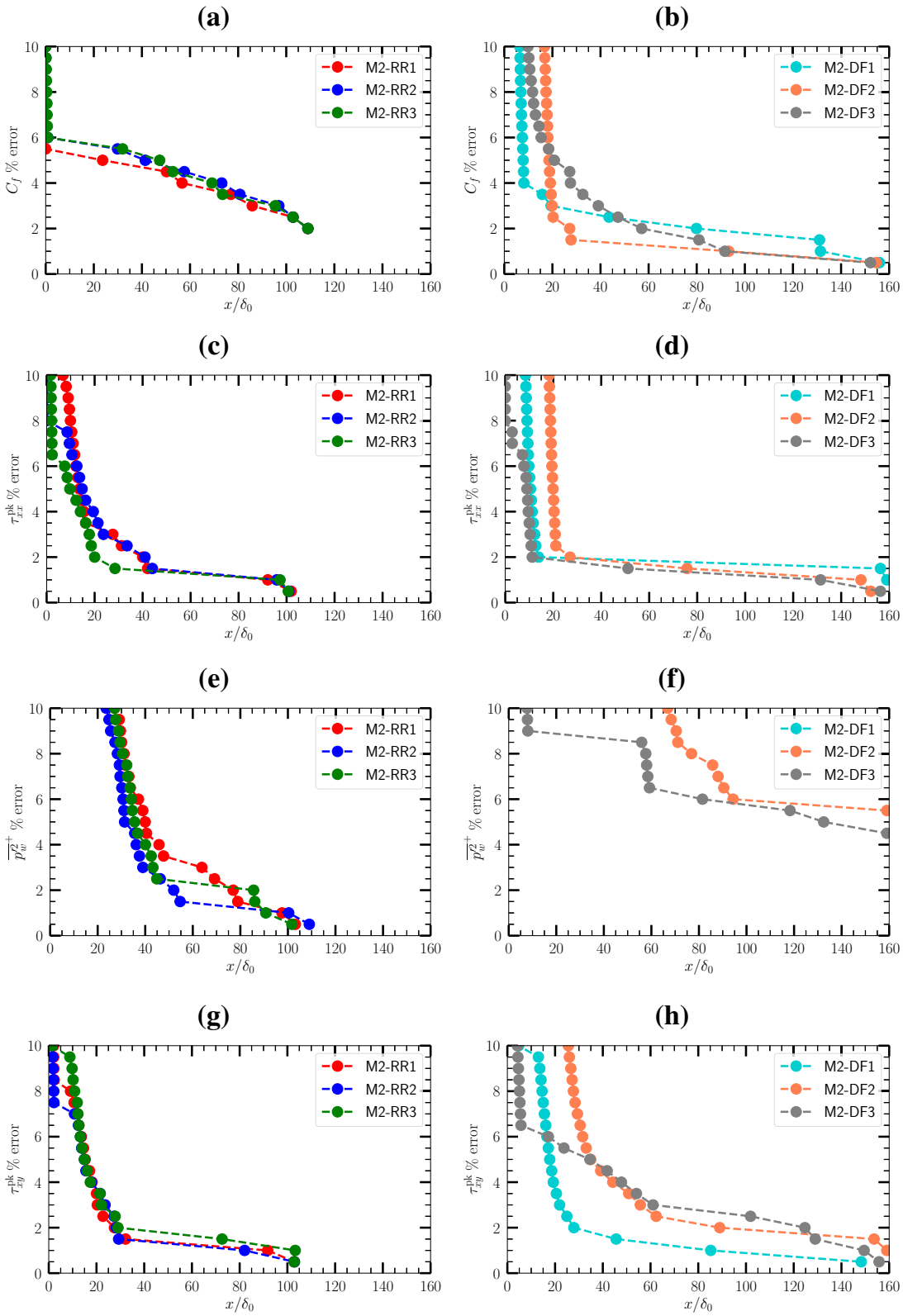

Fig. 19 Inflow length for supersonic flow cases as a function of target per cent error with respect to benchmark DNS for diagnostic quantities under scrutiny: (**a**, **b**) friction coefficient, (**c**, **d**) peak streamwise velocity variance, (**e**, **f**) wall pressure variance, and (**g**, **h**) peak turbulent shear stress. Left column RR, right column DF

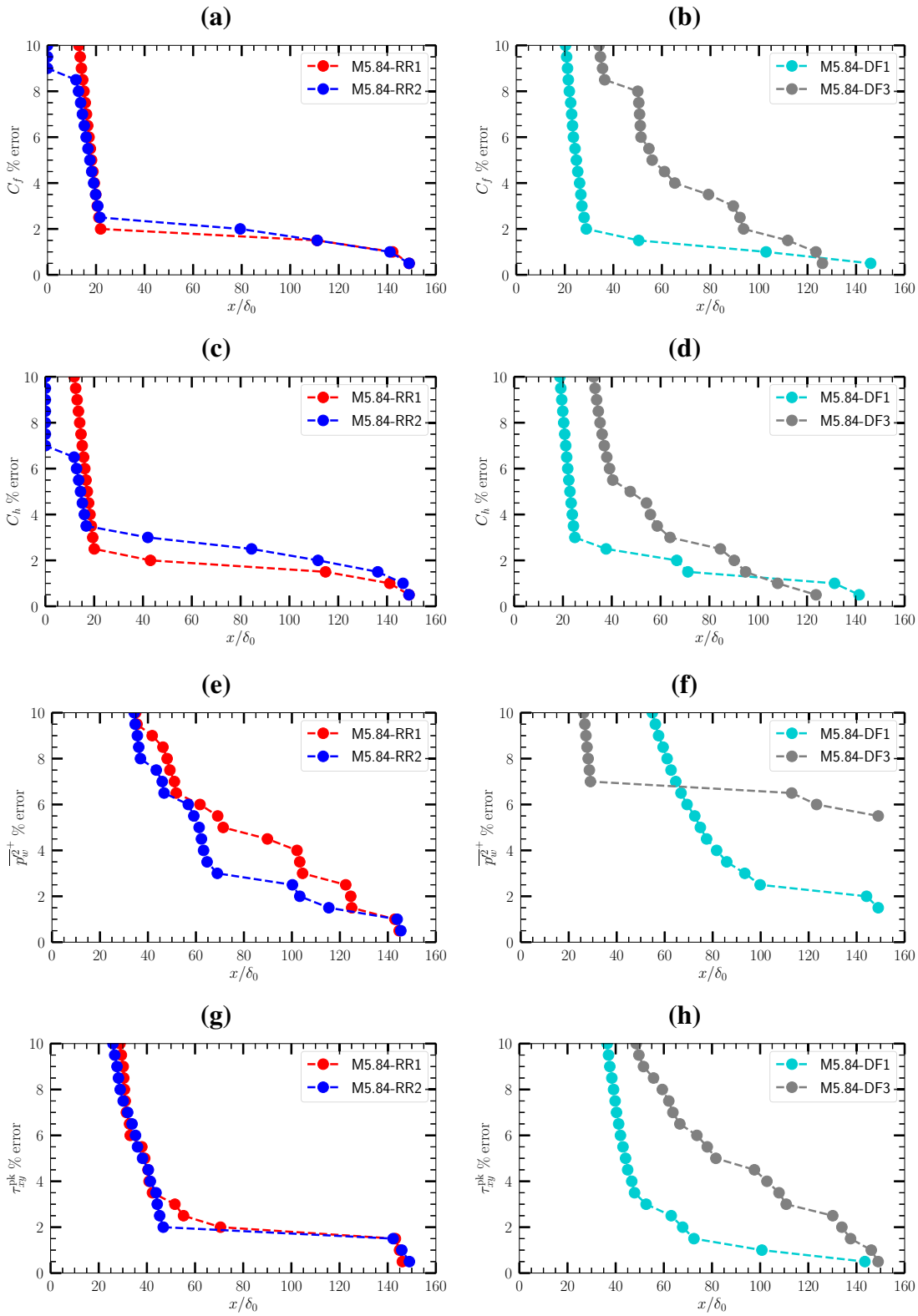

Fig. 20 Inflow length for hypersonic flow cases as a function of target per cent error with respect to benchmark DNS for diagnostic quantities under scrutiny: (**a**, **b**) friction coefficient, (**c**, **d**) heat transfer coefficient, (**e**, **f**) wall pressure variance, and (**g**, **h**) peak turbulent shear stress. Left column RR, right column DF

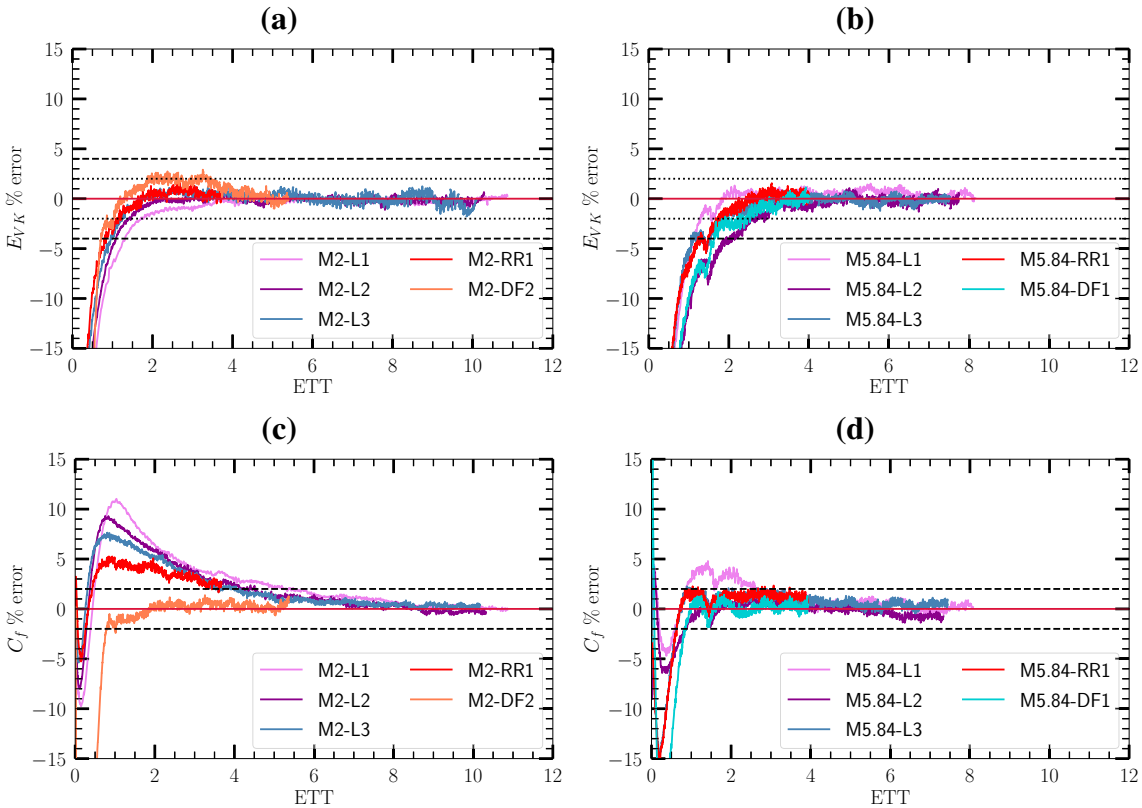

Fig. 21 Error in mean momentum balance (**a**, **b**) and in friction coefficient (**c**, **d**), as a function of number of eddy turnover times ETT for supersonic (**a**, **c**) and hypersonic (**b**, **d**) flow cases. The solid lines denote DNS data. The dashed lines in (**a**, **b**) denote $\pm 4\%$ error bands and the dotted lines $\pm 2\%$ error bands. The dashed lines in (**c**, **d**) denote $\pm 2\%$ error bands

for 2% tolerance. Baseline DF1, however, outperforms alternative implementations regarding the prediction of the peak shear stress, offering similar performance as RR in this respect.

These conclusions need some adaptation for the hypersonic flow cases (see Fig. 20). In particular, we find that this time the baseline DF inflow feeding, while retaining minor advantage over baseline RR in the prediction of the friction and heat transfer coefficients, also yields similar predictions of the wall pressure variance and of the peak turbulent shear stress. Regarding the proposed modifications, we find that the RR2 implementation yields some advantage in making RR less noisy, while worsening the prediction of C_h a bit. The beneficial effects of removing the streamwise velocity fluctuations in the DF3 implementation are instead lost, and instead we find significant deterioration in the prediction of friction and wall pressure variance. This is likely a result of very slow transition of the flow to a fully turbulent state, as suggested in Fig. 16b. Additional insight into the tendency of the flow statistics towards equilibrium can be gained by expressing the streamwise fetch from the inflow in terms of eddy turnover times, by exploiting Taylor's hypothesis [34] to define

$$\mathrm{ETT} = \frac{x/u_0}{\delta_0/u_\tau} = \frac{x}{\delta_0}\sqrt{\frac{C_f}{2}}. \tag{19}$$

This is done for the error in the mean momentum balance in Fig. 21a, b, which highlights that all simulations collapse after four ETT, regardless of the inflow seeding. All supersonic cases fall within $\pm 4\%$ error band after about one ETT, while the hypersonic cases after 1.5-2 ETT, in agreement with the literature results [11]. Regarding the friction coefficient, Fig. 21c, d shows that, whereas different inflow seeding yields different degree of accuracy in the initial transient, convergence to the benchmark distribution is basically complete after seven eddy turnover times for supersonic cases, and after about four turnover times in hypersonic cases, regardless of the seeding and of the inflow Reynolds number. As noted previously, the DF2 seeding yields faster adjustment of this particular parameter in the supersonic flow case, whereas baseline RR and DF seem to be most effective in the hypersonic flow case.

Recalling the goals of this study as originally stated, we believe that the main conclusions can be summarized as follows. First, we have established a standardized procedure to evaluate achievement of equilibrium conditions in numerical simulation of high-speed boundary layers. One of the conclusions in this respect is that no single criterion can be used to define the inflow length for arbitrary flow conditions, but rather each metric is subject to a different inflow length, which can also change as a result of the flow conditions. Perhaps surprisingly, we have found that the friction coefficient is particularly sensitive to inflow seeding, and it can bear memory of inflow seeding quite far from the inflow. An even more sensitive parameter is the wall pressure variance, which is typically overestimated from any inflow seeding technique, and which deserves special attention. Having each parameter to within a, say 1% error from true, does require extremely inflow lengths, certainly exceeding 100 inflow boundary layer thicknesses.

Surveying the current literature, it seems that very few studies have used such long domains, which raises questions about the reliability of reference data. For instance, we estimate that one of the commonly used databases [22], reports estimates of the friction coefficient which are about $1-2\%$ too high. On the other hand, other studies as by Wenzel et al. [43] may be regarded as essentially devoid of spurious inflow effects. In this respect, DNS in very long domains as reported here can provide a more robust benchmark. In particular, we have developed simple correlations for several flow diagnostics which we believe can be confidently used as a benchmark in code development, as well as for the development of alternative inflow seeding techniques.

Regarding the latter subject, we have attempted to develop modifications of the baseline RR and DF techniques. The results in this respect are only partially conclusive, but perhaps can provide inspiration for follow-up studies. Regarding the RR method, we have studied simplifications of the baseline algorithm which facilitate practical implementation, and which seem to offer predictions very close to the baseline approach. Regarding the DF method, which may be more relevant for application to practical engineering problems, we have found that the baseline version suffers from large overestimation of the wall pressure variance, owing to large noise generated at the inflow. Whereas this issue can be partially cured by suppressing the streamwise velocity fluctuations in the supersonic case, the same approach is not equally effective in hypersonic flow cases, as a result of delay in numerical transition. A possible strategy to mitigate the drawbacks of suppressing u' can be matching the turbulence kinetic energy content of the baseline DF implementation.

We expect that the present results can provide useful guidelines for the selection of inflow feeding techniques suitable for LES/DES of flow of industrial relevance, or in hybrid RANS/LES approaches [31,32,38]. Turbulence seeding is then used either at the inflow, or at the interface between scale-resolving and non-scale-resolving regions. In both cases a short inflow length is mandatory, not to interfere with physical phenomena of interest, e.g. shock wave impingement, flow control devices, wall curvature. The DF method is certainly a good candidate for the purpose as they can be adapted to complex geometries, even in the absence of homogeneous flow directions [1,42]. More importantly, the DF method can be easily incorporated into existing software. However, some weaknesses of DF should be overcome, including spurious pressure fluctuations from the inflow which can cause severe errors in aeroacoustic applications, and which can be minimized as shown here in the DF2-3 implementations. Finally, the computational overhead required by each inflow method must be taken into consideration as an important performance index. In this respect, we have found minimal difference in the wall clock time per iteration between DF and RR methods.

Overall, we find that the most important message from this paper is reiterating a caveat in the analysis of spatially developing flows, which despite careful numerical treatment require some inevitable adjustment length. In this respect, the error maps provided in Figs. 19 and 20 can provide useful guidance and feeling about the error bars to be expected for a given domain size, and for a given flow variable. We believe that all this information should be accounted for in the design of future large-scale DNS of high-speed wall-bounded flows, and in the development and assessment of novel inflow seeding techniques.

Acknowledgements This work was supported by TEAMAero Horizon 2020 research and innovation programme under grant agreement 860909 and by the Air Force Office of Scientific Research under grants FA9550-19-1-0210 and FA9550-19-1-7029. We acknowledge that the results reported in this paper have been achieved with computational resources of IscrB_THIPHRE and IscrB_3dSBLI projects, using the PRACE Research Infrastructure resource MARCONI100 based at CINECA, Casalecchio di Reno, Italy.

Data availability The data sets generated during and/or analysed during the current study are available from the corresponding author on reasonable request.

Funding Open access funding provided by Universitá degli Studi di Roma La Sapienza within the CRUI-CARE Agreement.

Declarations

Conflict of interest The authors report no conflict of interest.

References

1. Adler, M.C., Gonzalez, D.R., Stack, C.M., Gaitonde, D.V.: Synthetic generation of equilibrium boundary layer turbulence from modeled statistics. Comput. Fluids **165**, 127–143 (2018)
2. Bernardini, M., Modesti, D., Salvadore, F., Pirozzoli, S.: STREAmS: a high-fidelity accelerated solver for direct numerical simulation of compressible turbulent flows. Comput. Phys. Commun. **263**, 107906 (2021)
3. Chauhan, K.A., Monkewitz, P.A., Nagib, H.M.: Criteria for assessing experiments in zero pressure gradient boundary layers. Fluid Dyn. Res. **41**(2), 021404 (2009)
4. Chen, X., Hussain, F., She, Z.-S.: Non-universal scaling transition of momentum cascade in wall turbulence. J. Fluid Mech. **871** (2019)
5. Dhamankar, N.S., Blaisdell, G.A., Lyrintzis, A.S.: Overview of turbulent inflow boundary conditions for large-eddy simulations. AIAA J. **56**(4), 1317–1334 (2018)
6. Duan, L., Beekman, I., Martin, M.: Direct numerical simulation of hypersonic turbulent boundary layers. Part 2. Effect of wall temperature. J. Fluid Mech. **655**, 419–445 (2010)
7. Duan, L., Beekman, I., Martin, M.: Direct numerical simulation of hypersonic turbulent boundary layers. Part 3. Effect of Mach number. J. Fluid Mech. **672**, 245–267 (2011)
8. Erm, L.P., Joubert, P.N.: Low-Reynolds-number turbulent boundary layers. J. Fluid Mech. **230**, 1–44 (1991)
9. Farabee, T.M., Casarella, M.J.: Spectral features of wall pressure fluctuations beneath turbulent boundary layers. Phys. Fluids A **3**(10), 2410–2420 (1991)
10. Finley, P.: Static pressure in hypersonic nozzle boundary layers. AIAA J. **15**(6), 878–881 (1977)
11. Huang, J., Duan, L., Choudhari, M.M.: Direct numerical simulation of hypersonic turbulent boundary layers: effect of spatial evolution and Reynolds number. J. Fluid Mech. **937**, A3 (2022)
12. Jiménez, J., Hoyas, S., Simens, M.P., Mizuno, Y.: Turbulent boundary layers and channels at moderate Reynolds numbers. J. Fluid Mech. **657**, 335–360 (2010)
13. Kempf, A., Wysocki, S., Pettit, M.: An efficient, parallel low-storage implementation of Klein's turbulence generator for LES and DNS. Comput. Fluids **60**, 58–60 (2012)
14. Klein, M., Sadiki, A., Janicka, J.: A digital filter based generation of inflow data for spatially developing direct numerical or large eddy simulations. J. Comput. Phys. **186**(2), 652–665 (2003)
15. Lagha, M., Kim, J., Eldredge, J., Zhong, X.: A numerical study of compressible turbulent boundary layers. Phys. Fluids **23**(1), 015106 (2011)
16. Larsson, J.: Simple inflow sponge for faster turbulent boundary-layer development. AIAA J. **59**, 4271–4273 (2021)
17. Lund, T.S., Wu, X., Squires, K.D.: Generation of turbulent inflow data for spatially-developing boundary layer simulations. J. Comput. Phys. **140**(2), 233–258 (1998)
18. Martín, M.P.: Direct numerical simulation of hypersonic turbulent boundary layers. Part 1. Initialization and comparison with experiments. J. Fluid Mech. **570**, 347–364 (2007)
19. Musker, A.: Explicit expression for the smooth wall velocity distribution in a turbulent boundary layer. AIAA J. **17**(6), 655–657 (1979)
20. Pirozzoli, S.: Generalized conservative approximations of split convective derivative operators. J. Comput. Phys. **229**(19), 7180–7190 (2010)
21. Pirozzoli, S.: Numerical methods for high-speed flows. Annu. Rev. Fluid Mech. **43**, 163–194 (2011)
22. Pirozzoli, S., Bernardini, M.: Turbulence in supersonic boundary layers at moderate Reynolds number. J. Fluid Mech. **688**, 120–168 (2011)
23. Pirozzoli, S., Bernardini, M.: Probing high-Reynolds-number effects in numerical boundary layers. Phys. Fluids **25**(2), 021704 (2013)
24. Pirozzoli, S., Colonius, T.: Generalized characteristic relaxation boundary conditions for unsteady compressible flow simulations. J. Comput. Phys. **248**, 109–126 (2013)
25. Poggie, J., Bisek, N.J., Gosse, R.: Resolution effects in compressible, turbulent boundary layer simulations. Comput. Fluids **120**, 57–69 (2015)
26. Rai, M., Gatski, T., Erlebacher, G.: Direct simulation of spatially evolving compressible turbulent boundary layers. In: 33rd Aerospace Sciences Meeting and Exhibit, p. 583 (1995)
27. Ross, D.: Evaluation of the momentum integral equation for turbulent boundary layers. J. Aeronaut. Sci. **20**(7), 502–502 (1953)
28. Schlatter, P., Örlü, R.: Assessment of direct numerical simulation data of turbulent boundary layers. J. Fluid Mech. **659**, 116 (2010)

29. Schlatter, P., Örlü, R.: Turbulent boundary layers at moderate Reynolds numbers: inflow length and tripping effects. J. Fluid Mech. **710**, 5–34 (2012)
30. Schlatter, P., Li, Q., Brethouwer, G., Johansson, A.V., Henningson, D.S.: Simulations of spatially evolving turbulent boundary layers up to Reθ= 4300. Int. J. Heat Fluid Flow **31**(3), 251–261 (2010)
31. Schlüter, J., Pitsch, H., Moin, P.: Large-eddy simulation inflow conditions for coupling with Reynolds-averaged flow solvers. AIAA J. **42**(3), 478–484 (2004)
32. Shur, M.L., Spalart, P.R., Strelets, M.K., Travin, A.K.: Synthetic turbulence generators for RANS-LES interfaces in zonal simulations of aerodynamic and aeroacoustic problems. Flow Turbul. Combust. **93**(1), 63–92 (2014)
33. Sillero, J.A., Jiménez, J., Moser, R.D.: One-point statistics for turbulent wall-bounded flows at Reynolds numbers up to $\delta^+ = 2000$. Phys. Fluids **25**(10), 105102 (2013)
34. Simens, M.P., Jiménez, J., Hoyas, S., Mizuno, Y.: A high-resolution code for turbulent boundary layers. J. Comput. Phys. **228**(11), 4218–4231 (2009)
35. Smits, A., Matheson, N., Joubert, P.: Low-Reynolds-number turbulent boundary layers in zero and favorable pressure gradients. J. Ship Res. **27**(03), 147–157 (1983)
36. Smits, A.J., Dussauge, J.-P.: Turbulent Shear Layers in Supersonic Flow. Springer, Berlin (2006)
37. Spalart, P., Strelets, M., Travin, A.: Direct numerical simulation of large-eddy-break-up devices in a boundary layer. Int. J. Heat Fluid Flow **27**(5), 902–910 (2006). Special issue of the 6th International Symposium on Engineering Turbulence Modelling and Measurements—ETMM6
38. Spalart, P.R.: Detached-eddy simulation. Annu. Rev. Fluid Mech. **41**(1), 181–202 (2009)
39. Touber, E., Sandham, N.D.: Large-eddy simulation of low-frequency unsteadiness in a turbulent shock-induced separation bubble. Theor. Comput. Fluid Dyn. **23**(2), 79–107 (2009)
40. Trettel, A., Larsson, J.: Mean velocity scaling for compressible wall turbulence with heat transfer. Phys. Fluids **28**(2), 026102 (2016)
41. Urbin, G., Knight, D.: Large-eddy simulation of a supersonic boundary layer using an unstructured grid. AIAA J. **39**(7), 1288–1295 (2001)
42. Wang, R., Xiao, Z.: Influence of free-stream turbulence on the aerodynamic performance of a three-dimensional airfoil. AIP Adv. **11**(7), 075304 (2021)
43. Wenzel, C., Selent, B., Kloker, M., Rist, U.: DNS of compressible turbulent boundary layers and assessment of data/scaling-law quality. J. Fluid Mech. **842**, 428–468 (2018)
44. Wenzel, C., Gibis, T., Kloker, M., Rist, U.: Self-similar compressible turbulent boundary layers with pressure gradients. Part 1. Direct numerical simulation and assessment of Morkovin's hypothesis. J. Fluid Mech. **880**, 239–283 (2019)
45. Wenzel, C., Vogler, P., Peter, J.M.F., Kloker, M.J., Rist, U.: Application of a JPEG 2000-based data compression algorithm to DNS of compressible turbulent boundary layers up to $Re_\theta = 6600$. In: Nagel, W.E., Kröner, D.H., Resch, M.M. (eds.) High Performance Computing in Science and Engineering '20, pp. 295–313. Springer, Cham (2021)
46. Wray, A. A.: Minimal storage time advancement schemes for spectral methods. NASA Ames Research Center, California, Report No. MS, 202 (1990)
47. Wu, X.: Inflow turbulence generation methods. Annu. Rev. Fluid Mech. **49**, 23–49 (2017)
48. Xie, Z.-T., Castro, I.P.: Efficient generation of inflow conditions for large eddy simulation of street-scale flows. Flow Turbul. Combust. **81**(3), 449–470 (2008)
49. Xu, S., Martin, M.P.: Assessment of inflow boundary conditions for compressible turbulent boundary layers. Phys. Fluids **16**(7), 2623–2639 (2004)
50. Zhang, C., Duan, L., Choudhari, M.M.: Effect of wall cooling on boundary-layer-induced pressure fluctuations at Mach 6. J. Fluid Mech. **822**, 5–30 (2017)
51. Zhang, C., Duan, L., Choudhari, M.M.: Direct numerical simulation database for supersonic and hypersonic turbulent boundary layers. AIAA J. **56**(11), 4297–4311 (2018)